Applied Surface Science 416 (2017) 24–32

Contents lists available at ScienceDirect

Applied Surface Science

journal homepage: www.elsevier.com/locate/apsusc

Layer-by-layer assemblies of highly connected polyelectrolyte capped-Pt nanoparticles for electrocatalysis of hydrogen evolution reaction

Gonzalo E. Fenoy[a,b], Eliana Maza[a,c], Eugenia Zelaya[d], Waldemar A. Marmisollé[a,*], Omar Azzaroni[a]

[a] Instituto de Investigaciones Fisicoquímicas Teóricas y Aplicadas (INIFTA) – Departamento de Química – Facultad de Ciencias Exactas – Universidad Nacional de La Plata (UNLP), CONICET, 64 and 113, La Plata 1900, Argentina
[b] Instituto de Investigación e Ingeniería Ambiental, Universidad Nacional de San Martín, 25 de mayo y Francia, 1 piso, 1650 Buenos Aires, Argentina
[c] Soft Matter Nanotechnology Group, CIC biomaGUNE, Paseo Miramón 182, 20009 San Sebastián, Gipuzkoa, Spain
[d] CAB-CNEA, Av. Bustillo km 9.5 (8400), S.C. de Bariloche, CONICET, Argentina

ARTICLE INFO

Article history:
Received 19 November 2016
Received in revised form 8 April 2017
Accepted 12 April 2017

Keywords:
Layer-by-layer
Hydrogen evolution
Platinum nanoparticles
Electrochemistry
Electrocatalysis
Electroactive coatings

ABSTRACT

Herein we present a simple one-step method to produce polyelectrolyte-capped Pt nanoparticles able to be assembled into layer-by-layer arrays with a linear dependence of the amount of deposited material on the number of dipping cycles. The resulting supramolecular films where fully characterized by AFM, XPS and ATR-FTIR. The electrochemical evaluation by cyclic voltammetry showed good electrochemical connection between the nanoparticles in both acidic and neutral solutions. The films assembled on graphite electrodes showed catalysis of the H_2 production and the interconnection between nanoparticles proved to be effective up to 20 bilayers. Results presented here reveal an easy procedure to obtain stable arrays of well-dispersed electroactive 2 nm-diameter Pt nanoparticles on a variety of substrates with direct potential applications in energy conversion devices.

1. Introduction

Platinum is metal with exceptional catalytic properties that have made it widely useful in a variety of technological processes from cracking of petroleum and nitric oxide production to fuel cells [1–3]. Platinum catalyzes extremely important electrochemical reactions in energy production and conversion devices such as those involving the H_2 and O_2 reduction and evolution [4]. However, its elevated cost is a serious disadvantage and there is an urgent interest in replacing Pt or reducing the mass of Pt in the electrochemical applications. Metal nanoparticles (NPs) become a remarkable alternative as they offer large surface areas even for low metal load, keeping (or even enhancing) the electrocatalytic properties of the metal [5,6]. For its usage in electrochemical devices, NPs need to be supported on the electrode surface and even there, instability against dissolution and ripening can be a severe problem [7]. Capping NPs by polyelectrolytes has become a worthy strategy to deal with this, as polyelectrolytes can stabilize the NPs by suppression of aggregation or dissolution and they also confer alternative mechanisms to incorporate them in functional interfaces [8]. The control of composition and morphology of the electrochemical interfaces is an essential aspect of the design of electrochemical devices [9,10].

In the last decades, the manipulation of building blocks at the molecular level to generate organized materials at the nanoscale, often referred to as 'nanoarchitectonic' [11–14], has propelled the emergence of new hybrid functional coatings by combination of complementary components. Within the nanoarchitectonics, one of the simplest procedures to create hybrid interfaces consists of using layer-by-layer (LbL) assembly to integrate nanomaterials into films with nanometer-scale order [15]. This technique is based on the alternate deposition of multiply charged species to form multilayers in a controlled manner [16]. Although it was originally developed for polyelectrolytes, nowadays it has been extended to the incorporation of diverse nanostructures on a variety of surfaces [17,18]. In the case of electrochemical devices, such conjugation of

* Corresponding author.
E-mail address: wmarmi@inifta.unlp.edu.ar (W.A. Marmisollé).

http://dx.doi.org/10.1016/j.apsusc.2017.04.086
0169-4332/

building blocks aims the improvement of both their performance and chemical/mechanical stability.

Poly(diallyldimethylammonium chloride) (PDDA) is a non-electroactive cationic polyelectrolyte widely employed as robust building block in the construction of LbL arrays mainly due to the fact that its quaternary ammonium groups confer a high pH-independent positive charge [19,20]. In this sense, PDDA has been employed as counterpart in the construction of electroactive LbL arrays with several polymer-capped Pt NPs. Halaoui et al. studied the electrochemical behavior of polyacrylic acid-capped Pt NPs (Pt@PAA) assembled into LbL films employing PDDA as counterpart. The NPs showed electrocatalysis of the oxygen reduction reaction (ORR) and the hydrogen under potential deposition (UPD) peaks were clearly observed at low scan rates [21,22]. They also studied the hydrogen peroxide sensing by Pt@PAA assembled on PDDA. In this case, lower amounts of adsorbed NPs let to higher intrinsic sensitivities due to the overlapping of the diffusional profiles for denser NPs packings [23]. Halaloui has also shown that the polyvinylpyrrolidone (PVP)-capped 3–4 nm Pt NPs can be assembled in LbL arrays with PDDA [24]. The films showed electrocatalysis of the hydrogen evolution reaction and ORR and resulted to be stable to the oxidative potential cycling. A linear increase of the voltammetric charge of hydrogen UPD up to 10 bilayers was obtained for these assemblies. The capping of PVP has been also proved to be responsible for an enhancement of the electrocatalytic performance toward the formic acid and methanol oxidation reactions by inducing additional reaction pathways [25].

However, PDDA can be also employed as capping element on metal NPs. In this sense, PDDA has been showed to acts as stabilizer of Ag NPs [26] and as both reducing and capping agent in the synthesis of Au NPs by heat treatment of the aqueous solution of the precursors [27]. Even Jiang et al. have shown that Pt NPs synthesized by reductive heating in the presence of PDDA efficiently adsorb on negative Nafion membranes reducing the methanol crossover in fuel cells [28]. Furthermore, these NPs adsorbed on carbon black ink-coated electrodes showed electrocatalysis of the methanol oxidation reaction whose performance was dependent on the PDDA proportion [29]. PDDA-capped Pt NPs also showed higher catalytic currents for the oxygen reduction reaction (ORR) than NPs synthesized in the presence of other polyelectrolytes when assembled on Nafion-doped carbon ink-modified electrodes [30]. In a different approach, Pt NPs were synthesized inside LbL PDDA/PSS films by immersion in H_2PtCl_6 solution and subsequent chemical reduction of the exchanged complex anions. These arrays of NPs showed electrocatalysis of the methanol oxidation, with enhanced stability [31]. In other approach the electrostatic interaction between PDDA and $PtCl_6^{2-}$ was used for the preconcentration of Pt complexes and posterior reduction on PDDA-functionalized electrode surfaces [32]. The Pt nanostructures formed were electrocatalyzers of the hydrogen peroxide oxidation. More recently, a similar preconcentration step of the complex anions by PDDA has been employed in the decoration of graphene plates with Pt NPs for applications in electrocatalysis of the ORR [33,34] and methanol oxidation reaction [35,36]. Furthermore, it has been showed that PDDA can act as a modulator of shape and size of Pt nanocrystals (17–50 nm) grown from Pt NPs [37]. Nanocrystals showed enhanced stability and electrocatalytic activity toward the ORR, which were attributed to mitigation the Pt electro-oxidation and the modulation the electronic density on the nanocrystals by the PDDA respectively.

Undoubtedly, simplicity and low cost are desired characteristics of any method of production and assembly of NPs designed to be employed in technological applications. Here, we present a simple one-step method for preparing Pt NPs capped with poly(diallyldimethylammonium chloride) (Pt@PDDA NPs) yielding stable dispersions that can be directly employed for the construction of electrostatic LbL assemblies. As far as we are concerned, although some works on Pt@PDDA NPs were published, this is the first report on its LbL assembly and electrochemical characterization. Our results show that it is possible to produce a linear growing up of the films with a high level of electrochemical connection among the NPs within them, creating stable easily-made electroactive coatings with electrocatalytic activity toward the hydrogen evolution reaction.

2. Experimental

2.1. Chemicals

Poly(sodium 4-styrenesulfonate) (Mw 70 kDa) (PSS), poly(diallyldimethylammonium chloride) (20 wt% in H_2O, Mw 100–200 kDa) (PDDA) and polyethylenimine (Mw 10 kDa) (PEI) were purchased from Sigma–Aldrich.

Hydrogen hexachloroplatinate (IV) (8% in H_2O) was purchased from Sigma–Aldrich. Sodium borohydride was purchased from Lancaster. Potassium hexacyanoferrate (II) trihydrate was purchased from Biopack, potassium hexacyanoferrate (III) was purchased from Anedra. 4-(2-Hydroxyethyl)piperazine-1-ethanesulfonic acid (HEPES) was purchased from Sigma–Aldrich. Potassium hydroxide, potassium chloride and sulfuric acid were purchased from Anedra.

All chemicals were employed as received without further purification. All solutions were prepared with Milli-Q water (18.2 MΩ cm).

2.2. Instrumentation

Surface plasmon resonance (SPR) experiments were carried out by using a SPR Navi 210A instrument (BioNavis Ltd, Tampere, Finland). An electrochemistry cell (SPR321-EC, BioNavis Ltd.) was employed for all measurements. Gold sensors (BioNavis Ltd) were employed for SPR measurements were cleaned by immersion in boiling NH_4OH (28%)/H_2O_2 (100 vol) 1:1 for 15 min and then rinsed with water and ethanol. Injection was performed manually and SPR angular scans (785 nm laser) were recorded with no flow in the cell. Temperature was kept at 20 °C. All SPR experiments were processed using the BioNavis Data viewer software.

Dynamic light scattering (DLS) measurements were performed with a Zetasizer Nano (Nano ZSizer-ZEN3600, Malvern, U.K.) in water at 25 °C. The TEM and HRTEM observations were carried out in a cm200 UT FEI instrument operating at 200 keV. The ζ-potential was determined from the electrophoretic mobility measured by Laser Doppler Velocimetry with a Zetasizer Nano. The Smoluchowski approximation of the Henry equation was employed for calculations. Measurements were performed in triplicate using disposable capillary cells (DTS 1061 1070, Malvern) at 25 °C with a drive cell voltage of 30 V and employing the monomodal analysis method.

Atomic force microscopy (AFM) was performed with a Veeco Multimode AFM connected to a Nanoscope V controller was used to image the substrate. AFM measurements were performed in tapping mode in air using a TESP-V2 (Bruker, $K = 42\ N\ m^{-1}$) cantilever. AFM images were analyzed with the software WSxM 4.0 beta 8.2 [38].

X-ray photoelectron spectroscopy (XPS) was performed using a SPECS SAGE HR 100 system spectrometer. A Mg Kα (1253.6 eV) X-ray source was employed operating at 12.5 kV and 10 mA. Survey spectra were obtained with pass energy of 30 eV whereas 15 eV was employed for detailed spectra of C1s, N1s, and S2p regions. The take-off angle was 90° and operating pressure was 8×10^{-8} mbar. Quantitative analysis of spectra was carried out by using the Casa XPS 2.3. 16 PR 1.6 software, employing Shirley baselines and

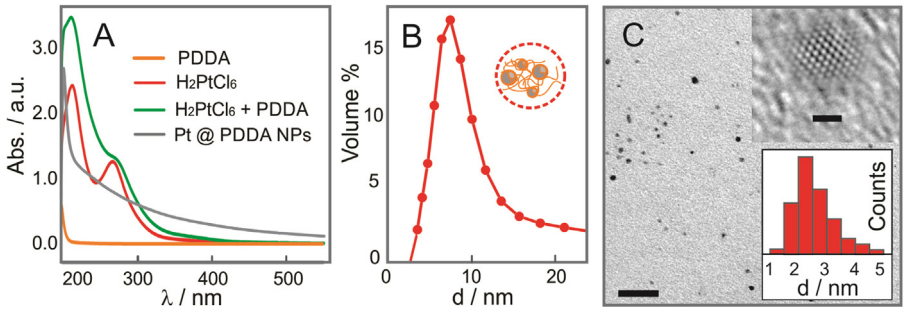

Fig. 1. (A) UV–visible spectra of Pt@PDDA NPs solution at different stages of the synthesis. (B) Volume distribution of the Pt@PDDA NPs in the synthesis solution by DLS. (C) TEM (scale bar 20 nm) and HRTEM (scale bar 1 nm) images of the NPs and histogram of the particle size distribution.

Gaussian\Lorentzian (30%) product functions. Surface-charging effects were corrected by setting the binding energy (BE) of the main component of the core level C1s at 284.5 eV. The full width at half maximum (fwhm) values were kept fixed for different components of a given element.

UV–visible spectroscopy was performed with a UV–VIS Agilent 8453E spectrometer employing quartz cells. Fourier transform infrared spectroscopy in the attenuated total reflection mode (ATR-FTIR) was performed using a Varian 600 FTIR spectrometer equipped with a ZnSe ATR crystal with a resolution of 4 cm^{-1}. Background-subtracted spectra were corrected for ATR acquisition by assuming a refractive index of 1.45 for all of the samples.

Cyclic voltammetry (CV) was performed using a Gamry REF600 potentiostat in a conventional three electrodes electrochemical cell. The counter electrode was a Pt wire and a Ag/AgCl (3 M NaCl) electrode was employed as reference. Potentials reported here are referred to this electrode. Electrodes were prepared by cutting graphite rods (Sigma–Aldrich, diameter = 3 mm, length = 150 mm) and then were polished with paper. In order to measure the electrochemically active surface area of the electrodes, we performed CV experiments with the Ferri/Ferro-cyanide couple. The mean electroactive area of the electrodes was 0.08 cm^2.

3. Results and discussion

3.1. Pt NPs synthesis and characterization

Pt@PDDA NPs were synthesized as follows. First, 125 μL of hexachloroplatinic acid solution was added into 250 mL of Milli-Q water. After stirring for 5 min, 66.5 mg of PDDA solution was added to obtain a molar ratio of 3:1 polyelectrolyte:Pt, followed by vigorous stirring for 80 min. Then, freshly prepared $NaBH_4$ solution (19.5 mg $NaBH_4$ dissolved in 2.5 mL H_2O) was added all at once. The color of solution slowly changed from pale yellow to dark brown, indicating the reduction of Pt ions and the formation of metallic Pt nanoparticles. The solution was stirred for 24 h.

The formation of the polyelectrolyte-stabilized Pt NPs was monitored by UV–vis spectrometry. Fig. 1(A) shows UV–vis spectra of samples taken at different times of the synthesis and a solution containing 0.164 mg mL^{-1} PDDA. The UV–vis spectrum of the PDDA solution only shows intense absorption bellow 200 nm. For the H_2PtCl_6 solution, there were two peaks at about 212 nm and 267 nm, characteristic absorbance of platinum complex of $PtCl_4^{-2}$ and $PtCl_6^{-2}$, respectively. The peak at 267 nm is the result of the ligand-to-metal charge-transfer transition in the $PtCl_6^{-2}$ ions [29]. After the addition of PDDA, there is a decrease in the peaks of H_2PtCl_6. The absorbance peak at 267 nm shifted to 269 nm, indicating the coordination of N atom in PDDA to Pt^{+4} ions (i.e. $PtCl_6^{-2}$ ions) [29]. After the reduction both peaks disappear and the intensity of scattering increased, suggesting that $PtCl_6^{-2}$ ions were reduced by $NaBH_4$ yielding particles. The UV–visible spectrum of the dark brownish final solution presents a typical scattering background (Fig. 1(A)).

3.2. Size and charge: DLS – TEM and ζ-potential

The synthesis solution was filtered (0.22 μm filter) and analyzed by DLS. Fig. 1(B) shows the volume distribution determined for the Pt@PDDA NPs. The volume size distribution has a mean value of 11 nm. TEM results of diluted Pt@PDDA NPs dispersion deposited by drop-casting on a TEM grid are also presented in Fig. 1(C). A bright field image of the Pt@PDDA NPs can be observed in this figure. The inset shows a HRTEM image of a FCC structure in [110] zone axis. The structure is compatible with the presence of Pt in the particles. The average diameter was determined to be 2.6 ± 0.6 nm for the metallic cores from the statistical analysis of the TEM images. Additional HRTEM results are presented in the SI file. Differences between DLS distribution and TEM histograms are caused by the fact that equivalent hydrodynamic diameters of the entire polyelectrolyte-capped NPs are determined in the DLS experiment.

The ζ-potential was determined in 0.1 M KCl (0.8 mL synthesis solution + 0.2 mL 0.5 M KCl). Values calculated from the electrophoretic mobility by employing the Smoluchowski's model for PSS, PDDA and Pt@PDDA NPs were −30, 46 and 19 mV respectively. Owing to the elevated surface charge dispersions of the Pt@PDDA NPs were bluntly stable, and no aggregation was observed even after several months of storage. Such stability and the positive surface charge of the Pt@PDDA NPs allow its direct LbL electrostatic assembly employing PSS as counter-polyelectrolyte. The construction of LbL assemblies of Pt@PDDA NPs from the synthesis solution on Au substrates is described in the next section.

3.3. LbL assembly

The LbL self-assembly on SPR gold sensors was initiated by injecting a positively charged PEI dispersion (1 mg mL^{-1}) to promote adhesion onto the substrate, giving an initial positive surface charge. This polyelectrolyte was selected for the initial functionalization because it also tightly bounds to other substrates, such as graphite or indium tin oxide (ITO). So, SPR results on Au could provide valuable information about the adsorption times required for the LbL construction of the assemblies on less expensive electrode materials. After the PEI step, negatively charged PSS dispersions (1 mg mL^{-1}) and positively charged Pt@PDDA NPs dispersions were alternately injected to form the LbL assembly on the gold surface. The synthesis solution was directly employed in the case of

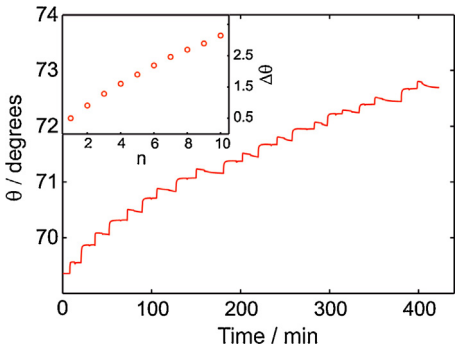

Fig. 2. Change in the minimum reflectivity angle of the SPR scan (measured at 785 nm) during the LbL formation of the supramolecular assemblies of Pt@PDDA with PSS on Au/PEI substrates. The inset shows the dependence of $\Delta\theta$ on the number of deposition cycles.

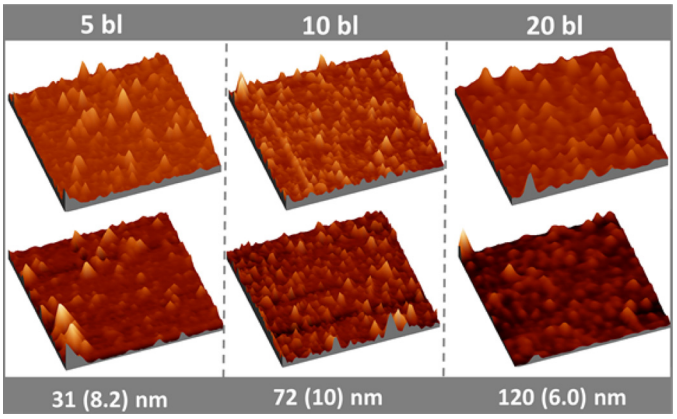

Fig. 3. AFM images (8 μm × 8 μm) of assemblies with different number of bilayers. Au/PEI/(PSS/Pt@PDDA)$_n$; for n = 5, 10 and 20. Thickness determined by AFM for each assembly is presented together with the RMS roughness (in brackets).

the Pt@PDDA NPs, without further purification steps. Pure water was injected after every layer to remove the excess of material. Each injection was successively introduced only after the signal of the previously injected component was stabilized (typically, 10–15 min). The minimum reflectivity angle is plotted as a function of time in Fig. 2. Although exact computation of the film thickness is not possible by SPR as metal nanoparticles within the film produce some scattering, changes in the reflectivity still allow monitoring the film growing up [39]. The adsorption seems to take place in one quick step, and no desorption process occurs when the system is flushed with water. The angle change for successive deposition steps suggests a linear dependence of the amount of deposited material on the number of deposition cycles (Fig. 2).

3.4. Characterization of the LbL assemblies

From the SPR results, the conditions for the LbL assembly were determined. LbL assemblies were also built onto Au-sputtered glass plates by dip-coating, soaking the electrodes alternately into the polyelectrolyte (PEI or PSS, 10 min) and Pt@PDDA NPs (20 min) dispersions, with water washing steps (5 min) between them (Scheme 1). After a desired number of deposition steps, the electrodes were dried with N_2. Topographic imaging by atomic force microscopy (AFM) indicated that the films are mainly homogenous with similar characteristics for assemblies with 5, 10 and 20 bilayers (Fig. 3). The root-mean-square surface roughness values are

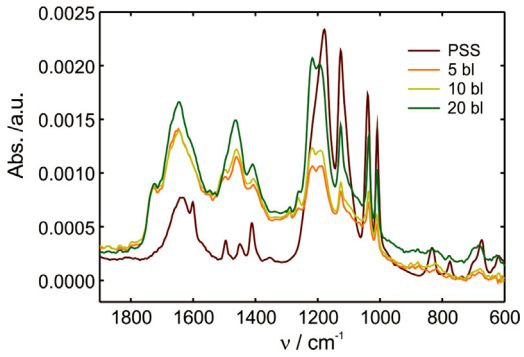

Fig. 4. ATR-FTIR spectra of assemblies of PSS and Pt@PDDA nanoparticles on Au.

Table 1
Components and relative composition determined from the fittings of the XPS results of the LbL assemblies.

	Pt4f		N1s		S2p	N1s/S2p
	Pt (0)	Pt(II/δ+)	−NH−	+NR$_4$	−SO$_3$	
BE/eV	71.2	73.5	399.5	402.2	167.1	
5 bl	70%	30%	25%	75%	100%	1.22
10 bl	65%	35%	21%	79%	100%	1.13
20 bl	78%	22%	15%	85%	100%	1.28

about 6–10 nm for all samples. The thickness of the dried films was estimated by scratching the surface with a wood stick and measuring the height of the step in the AFM (Fig. 3) (see Fig. SI 1). These results confirm the continuous growing of the LbL arrays even up to 20 deposition cycles, with similar structural characteristics. TEM and HRTEM images of the LbL assemblies are presented in the SI file. The TEM image for a 3-bilayers assembly does not show the presence of NPs aggregates which is consistent with a non-globular deposition of the metallic component.

Further chemical characterization of the films was performed by vibrational spectroscopy. The ATR-FTIR spectra of the LbL assemblies for different number of deposition cycles are presented in Fig. 4. The spectrum of PSS in this region is dominated by the typical sulfonate bands: a doublet at about 1126 and 1179 cm^{-1} assigned to the asymmetric stretching of the sulfonate group [40] and a band at 1039 cm^{-1} assigned to a symmetric stretching of the same group [40,41]. There is also a band at about 1009 cm^{-1} that has been assigned to in-place aromatic CH bending [40,42]. Finally, the band at 831 cm^{-1} has been assigned to the out-of-plane aromatic CH deformation [41]. In the case of the assemblies, the FTIR spectra confirm the presence of the sulfonate chemical moieties. The position of the sulfonate bands is basically the same, which shows that they remain in the salt form. Water of hydration manifests as a broad band at about 1400–1800 cm^{-1}. Higher signals are obtained for thicker films, but the relative intensities of the peaks remains the same which indicates that the chemical composition is preserved.

To gain additional information about the composition and chemical states within the films, XPS was performed. Representative results for an assembled film of 20 bilayers are presents in Fig. 5. Similar results for 5 and 10 bilayers are presented in the SI (Fig. SI 2–4). The XPS region of Pt4f core level can be fitted by two set of peaks as reported in Table 1. Owing to the spin–orbit coupling, the 4f core level shows a doublet coming from the different energy levels with $J = 7/2$ and $J = 5/2$. According to the degeneracy of these levels $(2J + 1)$, the area ratio $4f_{7/2}$: $4f_{5/2}$ is expected to be 4:3, so this ratio was fixed for fitting the results of the doublet. The separation between both peaks in the doublet was fitted to 3.3 eV. The first doublet has a BE of about 71.2 eV ($4f_{7/2}$) and can be assigned

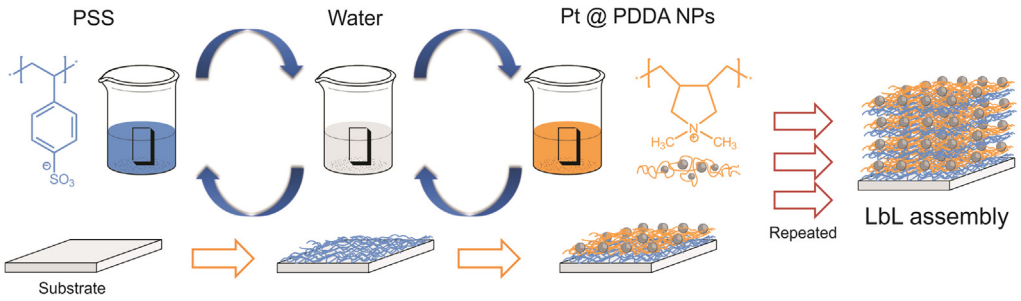

Scheme 1. Illustration of the layer-by-layer assembly process.

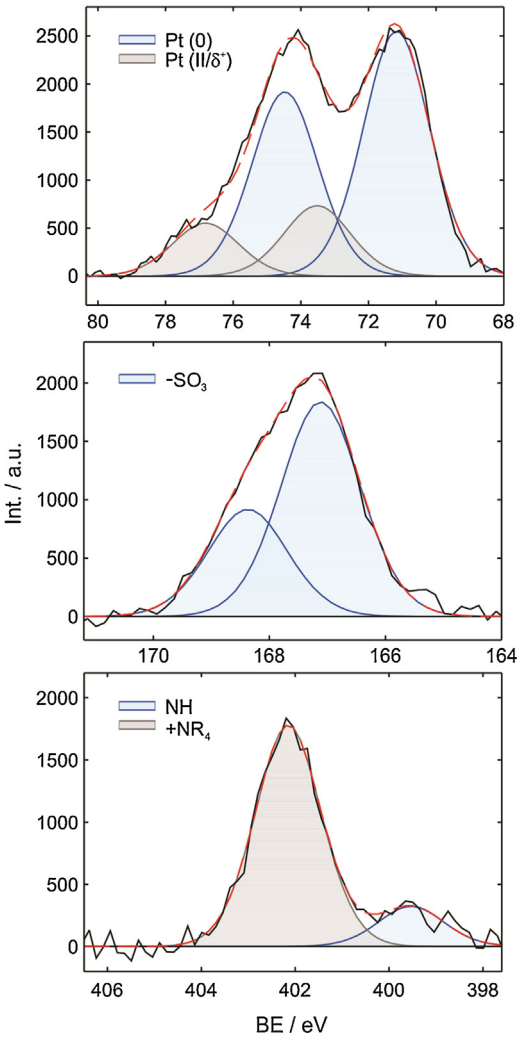

Fig. 5. XPS spectra and fittings for the Pt4f, S2p and N1s core level regions of a 20 bl assembly.

to metallic Pt (Pt(0)) [43,44]. Herein, it represents about the 70% of the Pt atoms. The other doublet appears at 73.5 eV ($4f_{7/2}$). The BE shift is consistent with Pt atoms having a loss of electron density (Pt δ^+). The BE separation between this components and that of Pt(0) (2.3 eV) is not so high as that measured for Pt(IV) species such as PtO_2 or $Pt(OH)_4$ (>3 eV) [44]. It has been reported that the presence of positive charges in the capping can shift the BE of Pt to higher energies [45], which indicates a strong interaction between the NPs surface and the capping. It could also be due to the formation of some Pt(II) species, as PtO, in the surface of the NPs [46]. The proportion of this additional component suggests that there is a high fraction of surface atoms in the NPs.

The XPS N1s core region can be fitted to with two components, as summarized in Table 1. The main component is that corresponding to the quaternary ammonium, which is the only species expected for the unmodified PDDA [35,45]. In the present case, there is an additional component at lower BE, which can be assigned to reduced nitrogen species (amine/imine) [47,48]. The presence of imine nitrogen species in PDDA has been also observed after the formation of Au NPs by heat treatment of $AuCl_4^-$ in basic solution [27], so it may be produced during the synthesis of the NPs with the $NaBH_4$. However, it has been also observed in similar systems even when no reducing treatment was performed, and it has been attributed to some remaining imine groups in the commercial PDDA [49]. XPS results of PDDA deposited on gold by drop-casting also present this imine component (Fig. SI 5), so we conclude that this contribution comes from some remaining groups in the polyelectrolyte.

Finally, the sulfur signal (S2p) appears at about 169 eV and can be fitted to a set of two bands at 167.1 and 168.3 eV, assigned to $S2p_{3/2}$ and $S2p_{1/2}$ respectively, with an integrated area ratio of 0.5 which takes into account the degeneration of these levels. Quantitative determination of the nitrogen to sulfur (N/S) atomic ratios was performed from the integrated intensity of the N1s and S2p signals. The effective relative cross-section was determined by measuring a sample of $(NH_4)_2S_2O_8$ powder in the same conditions as standard reference. Results presented in Table 1 indicate that the composition of the samples does not vary as further layers are deposited and it is consistent with a linear increment of the film thickness. Additionally, as the amount of sulfonate groups does practically coincide with the amount of positively charged quaternary ammonium, XPS results suggest that charge compensation is entirely carried out by the polyelectrolytes and there are not co-ions required within the films. The solutions for the dip-coating assembly were prepared without added salt to avoid the supra-linear film growing-up which generally deposits higher amounts of material in each LbL cycle with higher degree of stratification [50]. The more intimate contact between the counter-polyelectrolyte components might also allow higher degree of interdigitation, increasing the chances of connection between NPs deposited in successive cycles.

3.5. Electrochemical evaluation

The electrochemical oxidation of ascorbic acid (AA) has been extensively studied owing to the biochemical and industrial importance of AA and nowadays it has become a well-stablished redox system [51]. In this work, the electro-oxidation of AA onto the LbL modified electrodes was employed as a probe for testing the ability of the supramolecular assemblies to interact with biologically relevant species and electrochemically connect the electron transfer to the base electrode in neutral solution. On electroactive

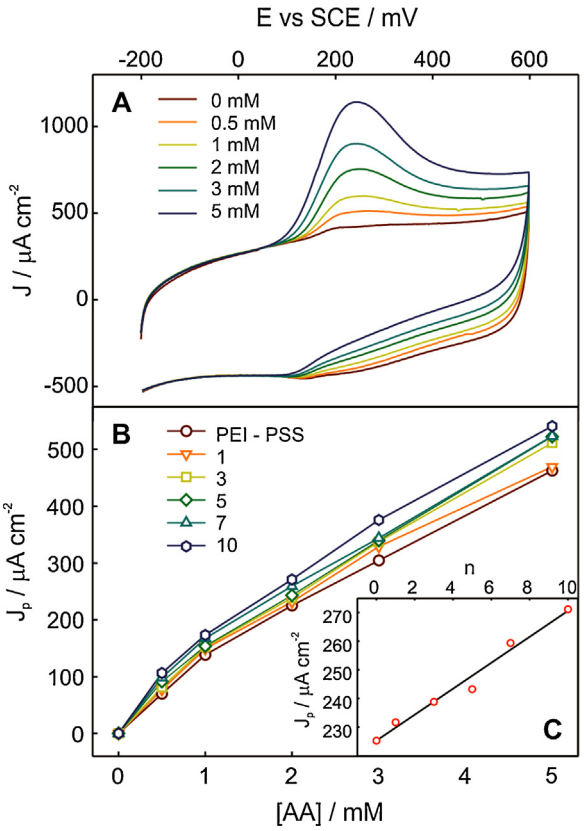

Fig. 6. Concentration dependence of the voltammetric response of an LbL-modified electrode in the presence of ascorbic acid.

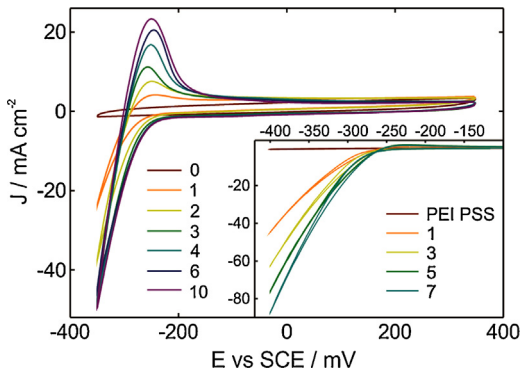

Fig. 7. Hydrogen evolution currents for graphite/PEI/PSS/(Pt@PDDA/PSS)$_n$ electrodes.

surfaces, the ascorbate anion is oxidized to dehydroascorbic acid (DHA) by an irreversible 2-electrons process [51]. However, when film-modified electrodes are employed, several mechanisms could be operative depending on the ability of the film components to mediate or catalyze the electron transfer and allow the electronic and ionic transport [52–54]. Voltammograms of the LbL modified electrodes show the typical dependence of diffusion-controlled irreversible electrochemical reactions [55]; i.e. the peak current depends linearly on the square root of the sweep rate, whereas the peak potential shifts linearly on the logarithm of the scan rate (Fig. SI 8). Higher bulk concentrations of AA lead to higher anodic currents (Fig. 6) as more molecules arrive to the surface by diffusion. However, as the bulk concentration increases, other steps rather than diffusion (electron transfer, charge transport within the film) could become rate limiting, which explains the non-linear dependence in Fig. 6(B) [52–54]. Charge transport could also become rate limiting for thicker films. Interestingly, in the case of these supramolecular films of Pt NPs, the voltammetric currents also increase with the number of assembled layers (Fig. 6). This indicates that the LbL assembly does not block the ionic transport nor the electronic transport to the surface as it usually occurs for thicker assembled films. Contrarily, the increase of the film thickness yields higher currents in the present case. Furthermore, the peak potential of the voltammograms is almost the same as in a blank electrode (graphite/PEI/PSS, see SI, Fig. SI 9) which indicates that the Pt@PDDA NPs do not add any catalytic effect toward the AA oxidation. Therefore, the higher currents may be assigned to a higher electroactive effective surface area caused by the deposition of highly connected metal nanoparticles onto the polyelectrolyte-functionalized graphite that increases the conductive pathways to the electrode.

Some kinetic effect could also be present. Similar increases in the diffusion-controlled voltammetric currents of reversible redox probes have been observed for other assemblies of metal NPs [56] or metal NPs and graphene sheets [57] in LbL films. In the latter case, it was assigned to synergic promotion of the electron transfer. Here, the relative increment in the peak current is higher for lower AA concentrations (see Fig. SI 10), where the diffusion-limitation is supposed to be more important. The current increases about 5% per assembled bilayer when AA concentration is 0.5 mM and less than 2% per bilayer for 2 mM. This suggests that the increase in the effective surface area electronically connected to the electrode would be the main factor. Nevertheless, beyond the operating mechanism, the supramolecular incorporation of additional layers of the Pt NPs on the electrode enhances its sensibility to AA as it yields higher oxidation currents.

3.6. Hydrogen evolution reaction and UPD

The H_2 evolution was studied by CV in N_2-bubbled 1 M H_2SO_4. As shown in Fig. 7, the presence of Pt NPs clearly induces the H_2 evolution as compared with the graphite electrode. Moreover, the currents remained the same after continuous potential sweeping, which indicates that the supramolecular assemblies were stable in these severe experimental conditions. The H_2 reduction and re-oxidation currents increase with the number of assembled layers, which indicates a good electrochemical connection between NPs in the succeeding layers. In the pseudo-polarization curves at 0.01 V s^{-1}, both the electrocatalysis and the effect of adding Pt NPs-containing layers are clearly observed.

The H under potential deposition (UPD) peaks were more noticeable after cycling the potential to high oxidative values. This procedure has been also reported for similar systems with PVP-capped Pt NPs, where the scan to higher positive potentials enhanced the hydrogen UPD peaks without changes in the peak position [24]. Fig. 8(A), shows the voltammograms on at 500 mV s^{-1} of graphite electrodes modified with different layers of assembly. Hydrogen UPD peaks are observed at this sweep rate. There are two peaks prior to the hydrogen evolution in the negative scan that are assigned to the reductive adsorption of H atoms in different atomic environments, sometimes referred to as strong (H_S) and weak (H_W) adsorption hydrogen [24]. On the other hand, after the molecular H_2 re-oxidation, there is a broad peak in the positive scan that is attributed to the oxidative desorption of H ad-atoms.

Remarkably, the voltammetric integrated charge of these peaks is a measure of the real surface area available for the UPD process in such a given condition. The voltammetric integrated charges of the hydrogen UPD for increasing number of Pt NPs deposition

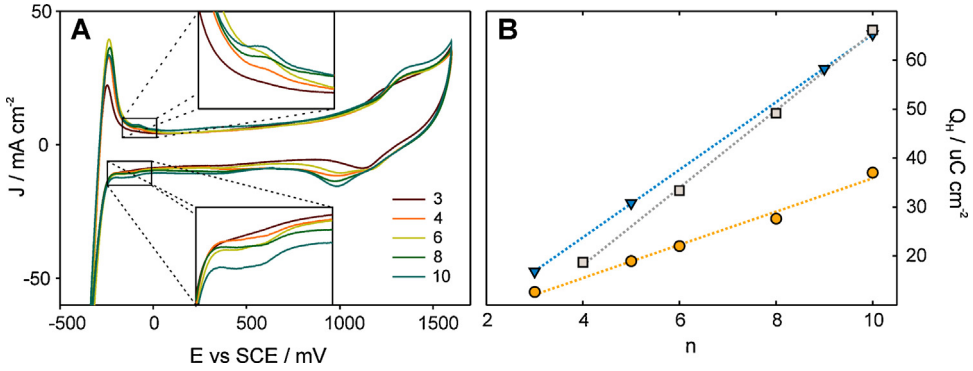

Fig. 8. (A) Hydrogen UPD peaks for graphite/PEI/PSS/(Pt@PDDA/PSS)$_n$ electrodes. (B) Hydrogen UPD integrated charges as a function of the number of deposition cycles of Pt NPs in graphite/PEI/PSS/(Pt@PDDA/PSS)$_n$ electrodes. Results for 3 different electrodes are presented.

cycles are shown in Fig. 8(B). Results for three different electrodes are presented. The linear increase in these charges proves that practically the same amount of electrically connected electroactive Pt NPs are incorporated in each LbL cycle. Results for assemblies up to 20 bilayers show the same linear behavior (see Fig. SI 11). The hydrogen adsorption/desorption process on the assembled Pt NPs requires transport of protons and counterions within the films across the polyelectrolyte domains and electronic hopping between the metallic domains. Voltammetric results in Fig. 8(A) show that mass and charge transport are feasible even at this high sweep rate. Furthermore, the increase in the hydrogen UPD peaks occurs without alteration of the peak potentials which means that transport is not blocked or hindered by the assembly of additional layers on the supramolecular films.

Repetitive potential cycling does not modify the UPD peaks, which means that the assemblies remain stable even when high positive potentials are attained. Compared with a clean polycrystalline Pt electrode, O_2 evolution is inhibited in the supramolecular assemblies (Fig. SI 12). Oxide peaks are also markedly shifts to more positive values, indicating that Pt NPs are more stable toward oxidation. Nevertheless, the oxide formation (or OH adsorption) voltammetric charge could also be employed as a measure of the amount of Pt within the assemblies. As it occurs for the hydrogen adsorption, there is a linear increment of the oxide formation voltammetric charge with the amount of assembled Pt NPs (see Fig. SI 13).

To gain some insight into the effect of the capping on the Pt electrochemistry, we also studied the voltammetric response of polycrystalline Pt before and after incubation in a 1 mg mL^{-1} PDDA solution for 30 min (see Fig. SI 14). The voltammetric response after PDDA adsorption shows a decrease and broadening of the hydrogen UPD peaks and oxide reduction as a consequence of the blockage of the surface. The peaks of clean Pt are just partially recovered by continuous potential cycling to the oxide formation region, which indicates a strong interaction with the metal surface. The presence of the PDDA also induces a shift of the Pt oxide formation to higher potential values. This stability against oxidation could be related to an electrostatic effect caused by the positive polyelectrolyte that hinders the formation of positive surface Pt species. This mechanism could be also operating on the Pt NPs arrays in the LbL-coated electrodes and could be the responsible for the enhanced stability toward oxidation. However, going to higher potentials also improves the observation of the hydrogen UPD peaks. This could be related to some reversible detachment of the capping positive groups by oxidation of the Pt NPs which would liberate sites for H adsorption. The fact that UPD peaks are less marked for low sweep rates could be then explained by the re-adsorption of the capping groups during the time elapsed between the oxide reduction and H adsorption. Some kind of capping restructuration accompanying the Pt oxide formation has been also hypothesized to occur in the case of PVP-capped Pt NPs in order to explain the enhancement of the UPD peaks with the increase in the anodic scan limit [24].

Although the observation of the hydrogen UPD peaks seems to be dependent on capping dynamics, hydrogen evolution is not affected. As shown in Fig. 7, cathodic currents are stable even at nearly steady-state conditions without the necessity of performing oxidation of the Pt NPs to induce electroactivity. Both the mechanical stability and the robust electroactivity toward the hydrogen evolution reaction become central aspects in the prospective implementation of the LbL supramolecular assemblies of Pt NPs in real energy conversion devices.

4. Conclusions

We have presented a simple one-step procedure for the synthesis of polyelectrolyte-capped Pt NPs. These NPs can be then assembled by LbL deposition yielding stable supramolecular films. The assembly results in a linear increase of the film thickness with the number of deposition cycles. The amount of NPs also increases linearly, which indicates a reproducible charge reversion after each cycle. The spectroscopic studies also indicate that the film growing up is homogenous and almost complete charge neutralization is probable to occur between the polyelectrolyte components due to the low ionic strength of the solutions employed for assembly. This allows an interdigitation of the assembled layers that produces an intimate contact of the metallic nanoparticles across the film. Henceforth, the Pt NPs present a high electrical connection that allows its implementation in electrochemical devices. The electrochemical evaluation of the supramolecular coatings also shows that effective mass and charge transport occur in the thickness of the films up to 20 bilayers of assembly. Both, the hydrogen UPD voltammetric charges and the AA electro-oxidation currents show that the electroactive area increases linearly on the number of bilayers. Moreover, the supramolecular films showed electrocatalysis of the H_2 evolution/oxidation reactions which are of great importance in energy conversion applications.

Acknowledgments

The authors acknowledge financial support from ANPCyT (PICT 2010-2554, PICT-2013-0905, PICT-2015-0239), Universidad Nacional de La Plata (PPID-X009), Consejo Nacional de Investigaciones Científicas y Técnicas (CONICET) (PIP 11220130100370CO), Marie Curie project "Hierarchical functionalization and assembly of Graphene for multiple device fabrication" (HiGRAPHEN) (Grant ref: 612704) and the Austrian Institute of Technology GmbH (AIT–CONICET Partner Lab: "*Exploratory Research for Advanced Technologies in Supramolecular Materials Science*" – Exp. 4947/11, Res.

No. 3911). W.A.M. and O.A. are CONICET fellows. G.E.F. gratefully acknowledges a Doctoral Scholarship from CONICET.

Appendix A. Supplementary data

Supplementary data associated with this article can be found, in the online version, at http://dx.doi.org/10.1016/j.apsusc.2017.04.086.

References

[1] N. Jung, D.Y. Chung, J. Ryu, S.J. Yoo, Y.E. Sung, Pt-based nanoarchitecture and catalyst design for fuel cell applications, Nano Today 9 (2014) 433–456.
[2] M.K. Debe, Electrocatalyst approaches and challenges for automotive fuel cells, Nature 486 (2012) 43–51.
[3] E. Antolini, Iron-containing platinum-based catalysts as cathode and anode materials for low-temperature acidic fuel cells: a review, RSC Adv. 6 (2016) 3307–3325.
[4] Y. Nie, L. Li, Z. Wei, Recent advancements in Pt and Pt-free catalysts for oxygen reduction reaction, Chem. Soc. Rev. 44 (2015) 2168–2201.
[5] Y. Xia, Y. Xiong, B. Lim, S.E. Skrabalak, Shape-controlled synthesis of metal nanocrystals: simple chemistry meets complex physics? Angew. Chem. Int. Ed. 48 (2009) 60–103.
[6] K.M. Bratlie, H. Lee, K. Komvopoulos, P. Yang, G.A. Somorjai, Platinum nanoparticle shape effects on benzene hydrogenation selectivity, Nano Lett. 7 (2007) 3097–3101.
[7] L. Li, L. Hu, J. Li, Z. Wei, Enhanced stability of Pt nanoparticle electrocatalysts for fuel cells, Nano Res. 8 (2015) 418–440.
[8] Y. Vu, J. Mark, Polymer-protected palladium nanoparticles. Morphologies and catalytic selectivities, Colloid Polym. Sci. 282 (2004) 613–619.
[9] M.M. Islam, S.H. Aboutalebi, D. Cardillo, H.K. Liu, K. Konstantinov, S.X. Dou, Self-assembled multifunctional hybrids: toward developing high-performance graphene-based architectures for energy storage devices, ACS Cent. Sci. 1 (2015) 206–216.
[10] N. Ashok Kumar, J. Baek, Electrochemical supercapacitors from conducting polyaniline–graphene platforms, Chem. Commun. 50 (2014) 6298–6308.
[11] K. Ariga, Y. Yamauchi, G. Rydzek, Q. Ji, Y. Yonamine, K.C.-W. Wu, et al., Layer-by-layer nanoarchitectonics: invention, innovation, and evolution, Chem. Lett. 43 (2014) 36–68.
[12] K. Ariga, Y. Yamauchi, M. Aono, Commentary: nanoarchitectonics – think about NANO again, APL Mater. 3 (2015) 61001.
[13] M. Aono, K. Ariga, The way to nanoarchitectonics and the way of nanoarchitectonics, Adv. Mater. 28 (2016) 989–992.
[14] K. Ariga, Q. Ji, W. Nakanishi, J.P. Hill, M. Aono, Nanoarchitectonics: a new materials horizon for nanotechnology, Mater. Horiz. 2 (2015) 406–413.
[15] T. Lee, S.H. Min, M. Gu, Y.K. Jung, W. Lee, J.U. Lee, et al., Layer-by-layer assembly for graphene-based multilayer nanocomposites: synthesis and applications, Chem. Mater. 27 (2015) 3785–3796.
[16] G. Decher, J.-D. Hong, Buildup of ultrathin multilayer films by a self-assembly process, 1 consecutive adsorption of anionic and cationic bipolar amphiphiles on charged surfaces, Makromol. Chemie. Macromol. Symp. 46 (1991) 321–327.
[17] Y.T. Park, J.C. Grunlan, Carbon nanotube-based multilayers, in: Multilayer Thin Film, Wiley-VCH Verlag GmbH & Co. KGaA, Weinheim, Germany, 2012, pp. 595–612.
[18] G. Rydzek, Q. Ji, M. Li, P. Schaaf, J.P. Hill, F. Boulmedais, et al., Electrochemical nanoarchitectonics and layer-by-layer assembly: from basics to future, Nano Today 10 (2015) 138–167.
[19] Y. Ahn, K.S. Yoo, L.-H. Kim, Y. Kwon, Development of biofuel cell adopting multiple poly(diallyldimethylammonium chloride) layers immobilized on carbon nanotube as powerful catalyst, Int. J. Hydrog. Energy (2016) 1–9.
[20] L. Du, F. Kong, G. Chen, C. Du, Y. Gao, G. Yin, A review of applications of poly(diallyldimethyl ammonium chloride) in polymer membrane fuel cells: from nanoparticles to support materials, Chin. J. Catal. 37 (2016) 1025–1036.
[21] Z.G. Estephan, L. Alawieh, L.I. Halaoui, Oxygen reduction at nanostructured electrodes assembled from polyacrylate-capped Pt nanoparticles in polyelectrolyte, J. Phys. Chem. C 111 (2007) 8060–8068.
[22] M.Z. Markarian, M. El Harakeh, L.I. Halaoui, Adsorption of atomic hydrogen at a nanostructured electrode of polyacrylate-capped Pt nanoparticles in polyelectrolyte, J. Phys. Chem. B 109 (2005) 11616–11621.
[23] P. Karam, L.I. Halaoui, Sensing of H_2O_2 at low surface density assemblies of Pt nanoparticles in polyelectrolyte, Anal. Chem. 80 (2008) 5441–5448.
[24] S. Jaber, P. Nasr, Y. Xin, F. Sleem, L.I. Halaoui, Assemblies of polyvinylpyrrolidone-capped tetrahedral and spherical Pt nanoparticles in polyelectrolytes: hydrogen underpotential deposition and electrochemical characterization, Phys. Chem. Chem. Phys. 15 (2013) 15223–15233.
[25] C. Susut, D.-J. Chen, S.-G. Sun, Y.J. Tong, Capping polymer-enhanced electrocatalytic activity on Pt nanoparticles: a combined electrochemical and in situ IR spectroelectrochemical study, Phys. Chem. Chem. Phys. 13 (2011) 7467–7474.
[26] A.B.R. Mayer, S.H. Hausner, J.E. Mark, Colloidal silver nanoparticles generated in the presence of protective cationic polyelectrolytes, Polym. J. 32 (2000) 15–22.
[27] H. Chen, Y. Wang, Y. Wang, S. Dong, E. Wang, One-step preparation and characterization of PDDA-protected gold nanoparticles, Polymer 47 (2006) 763–766.
[28] S.P. Jiang, L. Li, Z. Liu, M. Pan, H.L. Tang, Self-assembly of PDDA-Pt nanoparticle/nafion membranes for direct methanol fuel cells, Electrochem. Solid-State Lett. 8 (2005) A574.
[29] S.P. Jiang, Z. Liu, H.L. Tang, M. Pan, Synthesis and characterization of PDDA-stabilized Pt nanoparticles for direct methanol fuel cells, Electrochim. Acta 51 (2006) 5721–5730.
[30] Z.Q. Tian, S.P. Jiang, Z.C. Liu, L. Li, Polyelectrolyte-stabilized Pt nanoparticles as new electrocatalysts for low temperature fuel cells, Electrochem. Commun. 9 (2007) 1613–1618.
[31] X. Zhang, X. Zana, Z. Su, Polyelectrolyte multilayer supported Pt nanoparticles as catalysts for methanol oxidation, J. Mater. Chem. 21 (2011) 17783–17789.
[32] S. Chakraborty, C.R. Raj, Pt nanoparticle-based highly sensitive platform for the enzyme-free amperometric sensing of H_2O_2, Biosens. Bioelectron. 24 (2009) 3264–3268.
[33] Y. Shao, S. Zhang, C. Wang, Z. Nie, J. Liu, Y. Wang, et al., Highly durable graphene nanoplatelets supported Pt nanocatalysts for oxygen reduction, J. Power Sources 195 (2010) 4600–4605.
[34] W. He, H. Jiang, Y. Zhou, S. Yang, X. Xue, Z. Zou, et al., An efficient reduction route for the production of Pd-Pt nanoparticles anchored on graphene nanosheets for use as durable oxygen reduction electrocatalysts, Carbon 50 (2012) 265–274.
[35] D. Bin, F. Ren, Y. Wang, C. Zhai, C. Wang, J. Guo, et al., Pd-nanoparticle-supported, PDDA-functionalized graphene as a promising catalyst for alcohol oxidation, Chem. Asian J. 10 (2015) 667–673.
[36] Y.H. Xue, W.J. Zhou, L. Zhang, M. Li, S.H. Chan, Poly(diallyldimethylammonium chloride)-functionalized reduced graphene oxide supported palladium nanoparticles for enhanced methanol oxidation, RSC Adv. 5 (2015) 32983–32989.
[37] L. Du, S. Zhang, G. Chen, G. Yin, C. Du, Q. Tan, et al., Polyelectrolyte assisted synthesis and enhanced oxygen reduction activity of Pt nanocrystals with controllable shape and size, ACS Appl. Mater. Interfaces 6 (2014) 14043–14049.
[38] I. Horcas, R. Fernández, J.M. Gómez-Rodríguez, J. Colchero, J. Gómez-Herrero, A.M. Baro, WSXM: a software for scanning probe microscopy and a tool for nanotechnology, Rev. Sci. Instrum. 78 (2007) 13705.
[39] S. Tian, J. Liu, T. Zhu, W. Knoll, Polyaniline/gold nanoparticle multilayer films: assembly, properties, and biological applications, Chem. Mater. 16 (2004) 4103–4108.
[40] R.A. Weiss, A. Sen, C.L. Willis, L.A. Pottick, Block copolymer ionomers: 1. Synthesis and physical properties of sulphonated poly(styrene-ethylene/butylene-styrene), Polymer 32 (1991) 1867–1874.
[41] C.R. Martins, G. Ruggeri, M.A. De Paoli, Synthesis in pilot plant scale and physical properties of sulfonated polystyrene, J. Braz. Chem. Soc. 14 (2003) 797–802.
[42] D. Krishnamurti, R. Somashekar, Mesomorphic behaviour of dodecyl benzene sulfonic acid and its sodium salt, Mol. Cryst. Liq. Cryst. 65 (1981) 3–22.
[43] L. Qiu, F. Liu, L. Zhao, W. Yang, J. Yao, Evidence of a unique electron donor – acceptor property for platinum nanoparticles as studied by XPS, Langmuir 22 (2006) 4480–4482.
[44] F. Şen, G. Gökağaç, Different sized platinum nanoparticles supported on carbon: an XPS study on these methanol oxidation catalysts, J. Phys. Chem. C 111 (2007) 5715–5720.
[45] S. Zhang, Y. Shao, G. Yin, Y. Lin, Stabilization of platinum nanoparticle electrocatalysts for oxygen reduction using poly(diallyldimethylammonium chloride), J. Mater. Chem. 19 (2009) 7995.
[46] S. Porsgaard, L.R. Merte, L.K. Ono, F. Behafarid, J. Matos, S. Helveg, et al., Stability of platinum supported on SiO_2/Si(111): a high-pressure X-ray photoelectron spectroscopy study, ACS Nano. 6 (2012) 10743–10749.
[47] X. Song, Y. Ma, C. Wang, P.M. Dietrich, W.E.S. Unger, Y. Luo, Effects of protonation, hydrogen bonding, and photodamaging on X-ray spectroscopy of the amine terminal group in aminothiolate monolayers, J. Phys. Chem. C 116 (2012) 12649–12654.
[48] N. Graf, E. Yegen, T. Gross, A. Lippitz, W. Weigel, S. Krakert, et al., XPS and NEXAFS studies of aliphatic and aromatic amine species on functionalized surfaces, Surf. Sci. 603 (2009) 2849–2860.
[49] S. Wang, X. Wang, S.P. Jiang, Self-assembly of mixed Pt and Au nanoparticles on PDDA-functionalized graphene as effective electrocatalysts for formic acid oxidation of fuel cells, Phys. Chem. Chem. Phys. 13 (2011) 6883–6891.
[50] E. Maza, J.S. Tuninetti, N. Politakos, W. Knoll, S. Moya, O. Azzaroni, pH-responsive ion transport in polyelectrolyte multilayers of poly(diallyldimethylammonium chloride) (PDADMAC) and poly(4-styrenesulfonic acid-co-maleic acid) (PSS-MA) bearing strong- and weak anionic groups, Phys. Chem. Chem. Phys. 17 (2015) 29935–29948.
[51] A.M. Pisoschi, A. Pop, A.I. Serban, C. Fafaneata, Electrochemical methods for ascorbic acid determination, Electrochim. Acta 121 (2014) 443–460.
[52] W.A. Marmisollé, D. Gregurec, S. Moya, O. Azzaroni, Polyanilines with pendant amino groups as electrochemically active copolymers at neutral pH, ChemElectroChem 2 (2015) 2011–2019.
[53] A.M. Bonastre, M. Sosna, P.N. Bartlett, An analysis of the kinetics of oxidation of ascorbate at poly(aniline)-poly(styrene sulfonate) modified microelectrodes, Phys. Chem. Chem. Phys. 13 (2011) 5365–5372.

[54] P.N. Bartlett, E.N.K. Wallace, The oxidation of ascorbate at poly(aniline)–poly(vinylsulfonate) composite coated electrodes, Phys. Chem. Chem. Phys. 3 (2001) 1491–1496.
[55] A.J. Bard, L.R. Faulkner, Electrochemical Methods. Fundamentals and Applications, 2nd ed., Wiley, USA, 2001.
[56] M. Yang, Y. Yang, H. Yang, G. Shen, R. Yu, Layer-by-layer self-assembled multilayer films of carbon nanotubes and platinum nanoparticles with polyelectrolyte for the fabrication of biosensors, Biomaterials 27 (2006) 246–255.
[57] S. Liu, J. Yan, G. He, D. Zhong, J. Chen, L. Shi, et al., Layer-by-layer assembled multilayer films of reduced graphene oxide/gold nanoparticles for the electrochemical detection of dopamine, J. Electroanal. Chem. 672 (2012) 40–44.